Korean J. Chem. Eng., 38(5), 952-965 (2021)
DOI: 10.1007/s11814-021-0756-x

pISSN: 0256-1115
eISSN: 1975-7220

Facile synthesis and characterization of $WO_3/CuWO_4$ nanocomposites for the removal of toxic methylene blue dye

Thilagavathi Thiyagarajan*,†, Venugopal Deivasigamani*, Marnadu Raj, Chandrasekaran Joseph**, Thangaraju Dheivasigamani***, Baskaran Palanivel****, Mohamed S. Hamdy*****, and Mohd. Shkir******

*Department of Physics, Gobi Arts & Science College, Gobichettipalayam - 638453, Erode, Tamilnadu, India
**Department of Physics, Sri Ramakrishna Mission Vidyalaya College of Arts and Science, Coimbatore - 641020, Tamilnadu, India
***Nano-crystal Design and Application Lab (n-DAL), Department of Physics, PSG Institute of Technology and Applied Research, Coimbatore - 641062, Tamil Nadu, India
****Department of Physics and Nanotechnology, SRM Institute of Science and Technology, Kattankulathur, Kancheepuram 603203, Tamil Nadu, India
*****Catalysis Research Group (CRG), Department of Chemistry, College of Science, King Khalid University, P.O. Box 9004, Abha 61413, Saudi Arabia
******Advanced Functional Materials & Optoelectronics Laboratory, Department of Physics, College of Science, King Khalid University, Abha - 61413, Saudi Arabia
(*Received 25 August 2020 • Revised 25 December 2020 • Accepted 29 January 2021*)

Abstract−Pure tungsten oxide (WO_3) nanoparticles (NPs) and WO_3/copper tungstate ($CuWO_4$) nanocomposites (NCs) were prepared by varying copper content from (5-20 wt%) via the co-precipitation process. XRD results reveal that the structural parameters of $WO_3/CuWO_4$ NCs have been strongly affected via Cu doping. Morphology of synthesized WO_3 was noticed to be distinct and particle size was significantly reduced through Cu doping confirmed by employing HRTEM studies. Elemental purity of as synthesized products, elucidated from EDX and XPS analyses, reveals that $WO_3/CuWO_4$ nanocomposites contain W, O and Cu elements only. Also, FT-IR spectra and its corresponding assignments indicate the existence of $WO_3/CuWO_4$. UV-Visible study shows that $WO_3/CuWO_4$ composites have narrow bandgap compared to pure WO_3. Photoluminescence spectral peaks intensity of NCs displays a decreasing trend, which supports the enhanced photocatalytic activity. The results clearly show that 20 wt% Cu incorporated WO_3 sample exhibits better photocatalytic nature than that of pure WO_3 and will be more applicable in purify the water.

Keywords: $WO_3/CuWO_4$ NCs Synthesis, X-ray diffraction, HRTEM/SAED, XPS, Optical Properties, Photocatalytic Activity

INTRODUCTION

The presence of non-biodegradable, carcinogenic synthetic toxic organic dyes in textile and leather industry effluents pollutes water resources like lakes and rivers [1,2]. In the present circumstances, inexpensive and large scale effective clean water production technologies are essential to supply clean water to humans as well as aquatic organisms. In fulfilling the increasing clean water demand, a simple and eco-friendly semiconductor photocatalytic green chemical technique is extensively acknowledged [3,4]. In this aspect, popular semiconductor photocatalysts such as TiO_2, α-Fe_2O_3, NiO, ZnO, SnO_2 and WO_3 have been utilized and studied for their photocatalytic degradation of toxic organic dyes. Among the extensively investigated transition metal oxide semiconductors, WO_3 is an important widely tunable bandgap (around 2.8 eV) n-type material. It is found to be an appropriate photocatalytic material owing to its harmlessness, earth-abundance, highly photo-active and able to respond ultraviolet and visible lights to degrade toxic dyes [5]. WO_3 has extensive applications in diverse fields, such as batteries based on Li-ions [6], sensing of toxic gases [7], and heterogeneous catalyst [8]. Also, WO_3 has several polymorphs as a result of temperature and the method of synthesis. Among the existing polymorphs, the monoclinic phase is the most stable and always shows enhanced photocatalytic activity compared to other phases of WO_3 [9]. Moreover, WO_3 exhibits nanorods [10], nanoplates [11] and nanowire [12] morphologies. Due to these excellent reasons, WO_3 has been synthesized from various techniques, including impregnation method [13], hydrothermal synthesis [14], co-precipitation [15], molten salts process [16] and sol-gel [17] method. From all the available physical and chemical methods, the co-precipitation method is advantageous due to its cost-effectiveness and quick formation of nanoparticles [18]. Regrettably, the fast recombination frequency of electron-hole pairs generated under light limits the photocatalytic degradation efficiency of pure WO_3 nanoparticles. To overcome the drawbacks gone through pure WO_3, low cost, chemically and thermally stable n-type semiconductor copper tungstate

†To whom correspondence should be addressed.
E-mail: thilagavathi01@gmail.com

($CuWO_4$) forms the heterojunction coupling with WO_3 may enhance the separation of photo induced charge carriers (e^--h^+) [19]. As a result, the as-formed $WO_3/CuWO_4$ nanocomposites have proven to be a successful photocatalyst. In view of that, Salimi et al., reported the photocatalytic performance of $CuWO_4/WO_3$ heterostructures [20]. Neto et al. studied the photocatalytic properties of $CuWO_4$, $CuWO_4/WO_3$ and $CuWO_4$/CuO powders by sonochemical method [21]. Chen et al. reported the photocatalytic activity of WO_3 through $CuWO_4$ for phenol degradation [22]. The photocatalytic degradation of cationic toxic dyes by WO_3 doped with other metals has been reported by many researchers.

Accordingly, Aslam et al. prepared $WO_3/CdWO_4$ as photocatalyst and studied organic contaminants degradation under VIS light [23]. Tahir et al. reported the improved photocatalytic action g-WO_3 for producing hydrogen [24]. Ismail et al. studied WO_3/graphene as photocatalyst below VIS light for MB degradation [25]. Yu et al. reported AgCl/WO_3 composite microrod photocatalysts prepared by hydrothermal method [26].

In the present work, we prepared pure WO_3 nanoparticles and $WO_3/CuWO_4$ nanocomposites with Cu content (5-20 wt%) via the co-precipitation method. Detailed structural, surface morphological and optical characterizations were done. In addition, photocatalytic activity and the possible mechanism responsible for photocatalytic degradation of MB by the prepared samples were also proposed based on the experimental observations. We report that the heterojunction structured $WO_3/CuWO_4$ nanocomposites offer enhanced photocatalytic degradation efficiency than pure WO_3 nanoparticles.

INVESTIGATIONAL DETAILS

1. Preparation of Pure WO_3 and $WO_3/CuWO_4$ Nanocomposites

To synthesize pure WO_3 NPs and $WO_3/CuWO_4$ NCs, a simple and environmentally friendly co-precipitation technique was preferred, and the detailed process is illustrated in Fig. 1. In a typical synthesis, 0.5 M of Sodium tungstate dihydrate ($Na_2WO_4{\cdot}2H_2O$) of M.W 329.86 g/ml (AR grade) was dissolved in 40 ml deionized water and within a few minutes a transparent solution was attained. This transparent solution turned to pale yellow color when 5 ml of concentrated HCl was added. Afterwards, Cu $(NO_3)_2{\cdot}3H_2O$ with (0-20 wt%) acting as a Cu doping agent dissolved in deionized water was added to the total solution. Then the complete solution was stirred continuously for 2 hours at 80 °C in a temperature-controlled magnetic stirrer and after cooling to 300 K, a bluish-yellow colored precipitate/powder was formed. Further, this precipitate was washed with acetone, ethanol followed by deionized water numerous times to eliminate scum. To eliminate moisture, the cleaned precipitate was kept in an oven for 6 hours at 60 °C. Finally, the samples were annealed at 600 °C in an air atmosphere using a muffle furnace for an hour. After annealing, WO_3 samples were ground for 30 minutes using mortar and pestle. From the above-synthesized procedure, 0 wt% Cu gives pure WO_3 and (5-20 wt%) gives $WO_3/CuWO_4$ nanopowders. These powders were stored in airtight, dust-free vials for further characterization.

2. Photocatalytic Activity Measurement

The prepared WO_3 NPs can be used to remove pollutants such as dye molecules present in water. For this experiment, cationic Methylene blue (MB) was taken as a model pollutant and the actual concentration of the prepared MB dye was 10 mgL^{-1}. From the above quantity of dye solution, only 50 ml was taken and 0.020 g of pure WO_3 NP and $WO_3/CuWO_4$ NCs were separately dispersed over this solution. To measure the decolorization ability of the WO_3, $WO_3/CuWO_4$ catalysts, the catalysts and dye solution were irradiated with 125 W high-pressure mercury lamp UV light source with a spectral peak centered at 365 nm (UV-A) using Heber photoreactor (Model: HML-COMPACT-SW-MW-LW 888). The catalyst and blue colored dye solution were filled in a cylindrical borosilicate glass tube and inserted in the corresponding holder with photoreactor chamber. This catalyst - blue-colored dye solution, suspension aerated constantly and changed to colorless within 80 minutes, shows the removal of dye by the WO_3 NPs and $WO_3/CuWO_4$ NCs after irradiation of UV-A source. During irradiation, the catalyst - dye suspension was collected every 20 minutes of time intervals. The absorption spectrums of the as collected samples were recorded using JASCO spectrophotometer.

3. Characterization Techniques

Phase and purity of all the samples were investigated through PANalytical X' Pert PRO X-ray diffractometry (XRD) having radiation of CuKα with λ=1.5406 A°. The shape and structure were

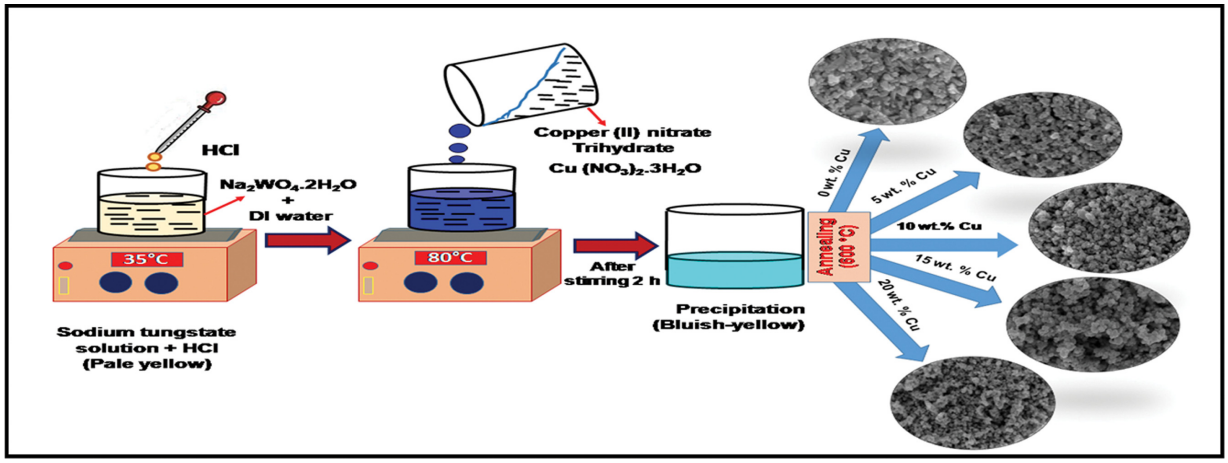

Fig. 1. Schematic illustration for preparing pure WO_3 nanoparticles and $WO_3/CuWO_4$ nanocomposites.

inspected by a Field emission SEM (SIGMA HV - Carl Zeiss) and high-resolution TEM-JEM 2100 from JEOL. The elemental inspection was done through EDS/SEM device. The chemical composition of elements was examined via the XPS spectrophotometer (Kratos Analytical) equipped with a monochromatic AlKα source of radiation (1,486.6 eV). The Avatar 370-FT-IR spectrometer was employed to measure the spectra over 400 to 4,000 cm^{-1} region with a firmness of 4 cm^{-1}. Varian Cary 5000 UV-Vis-NIR DR spectrophotometer was used to measure reflectance profiles. Photoluminescence was studied by the Varian Cary Eclipse system.

OUTCOMES AND DIALOGUE

1. XRD Study

Fig. 2(a) illustrates the XRD profiles of annealed pure WO_3 NPs and WO_3/$CuWO_4$ NCs with various amounts of Cu content (0-20 wt%). It is apparent from the Fig. 2(a) that pure WO_3 NPs exhibits a well-resolved intensive triplet diffraction peaks at 2θ=23.30°, 23.71° and 24.48° indexed as (002), (020) and (200) planes, respectively. All the diffraction planes correspond to monoclinic structure and compatible with JCPDS # 83 - 0950. When copper content was introduced into pure WO_3, the most predominant triplet peak was suddenly reduced in its intensity, shown in Fig. 2(a). Moreover, the shifting of triplet peak towards the lower angle diffraction side was observed for all WO_3/$CuWO_4$ NCs depicted in Fig. 2(b). This peak shift may occur due to the ionic radius dissimilarity of the host WO_3 (W^{6+}=0.65 A°) and the guest (Cu^{2+}=0.73 A°) and also lattice distortion created by higher ionic radius differences between the W^{6+} and Cu^{2+} ions. The diffraction peaks at 2θ position 26.8°, 33.39°, 34.27°, 41.95°, 47.40°, 46.83°, 49.99°, 50.14°, 52.08°, 53.84°, 56.01° and 58.71° appeared in pure were suppressed and disappeared in WO_3/$CuWO_4$ NCs samples. Interestingly, one new peak was recorded at 43.11° (denoted by *) having monoclinic structure that matches well with JCPDS 83-0950. Additionally, triclinic structured $CuWO_4$ peaks were formed at 26, 30.26, 31.86, 32.14 and 35.61° denoted as dot confirmed with JCPDS card No: 01-073-1823. All these interesting changes in the XRD pattern proved that copper has the utmost impact on the structural parameters of WO_3/$CuWO_4$ NCs.

The average values of crystallite size (D), dislocation concentration (δ), and strain (ε) of the pure and WO_3/$CuWO_4$ NCs were obtained using below formulae [27-32] and provided in Table 1.

$$D_{ave} = \frac{k\lambda}{\beta\cos\theta} \quad (1)$$

$$\delta_{ave} = \frac{1}{D^2} \quad (2)$$

$$\varepsilon_{ave} = \frac{\beta\mathrm{Cot}\theta}{4} \quad (3)$$

$$SF_{ave} = \left[\frac{2\pi^2}{45(3\tan\theta)^{1/2}}\right]\beta \quad (4)$$

The acquired results of D for pure WO_3 NPs and WO_3/$CuWO_4$

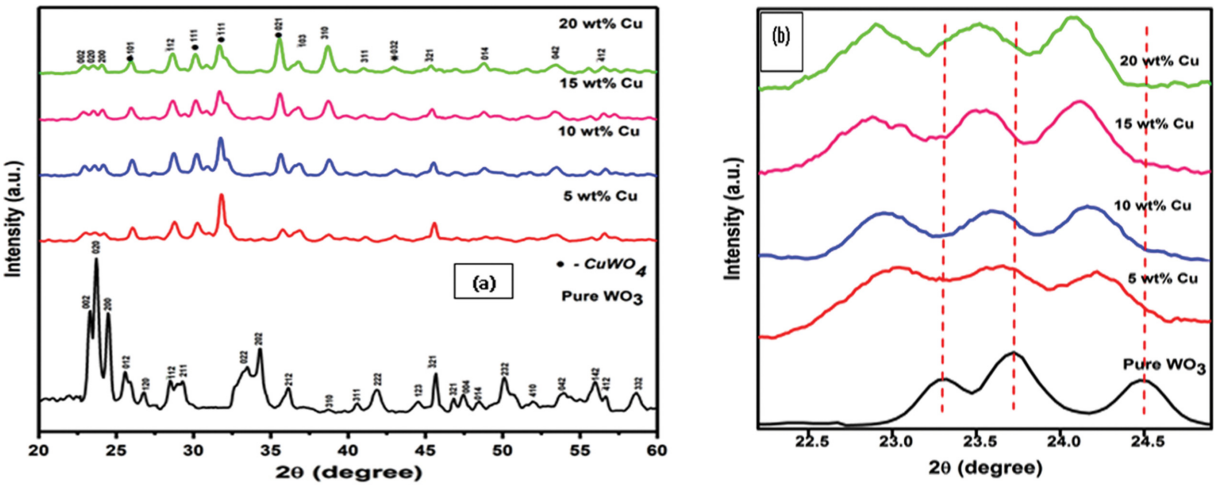

Fig. 2. (a) XRD patterns and (b) peak shift patterns of pure WO_3 nanoparticles and WO_3/$CuWO_4$ nanocomposites.

Table 1. Average structural parameters calculated for pure WO_3 nanoparticles and WO_3/$CuWO_4$ nanocomposites

Cu concentration (wt%)	Grain size (D_{ave}) nm	Dislocation density (δ_{ave})×10^{-3} nm^{-2}	Micro strain (ε_{ave}) 10^{-3}	Stacking fault (α_{ave})×10^{-3}
0	34.42	1.15	3.52	2.05
5	32.81	1.23	4.22	2.09
10	30.18	1.27	4.28	2.19
15	29.44	1.51	4.6	2.32
20	27.49	1.55	4.66	2.44

NCs are approximately 34.42, 32.81, 30.18, 29.44 and 27.49 nm, respectively. These sorts of decrease in crystallite size perceptibly illustrate the strong incorporation of Cu^{2+} ions into W^{6+} lattice positions. Our result agrees well with the previously reported results [33,34]. This decrease in size might be beneficial for transferring of charge carriers generated by light to surface where it might have a considerable role for enhancing the photocatalytic nature. The mean values of δ, ε and α increase continuously on increase of Cu dopant from 0 to 20 wt%.

2. FE-SEM Analysis

Fig. 3 FESEM study was employed to evaluate the surface morphological information and structure of the pure WO_3 NPs and $WO_3/CuWO_4$ NCs with increase in Cu^{2+} content from 5-20 wt% are shown in Fig. 3(a)-(e). The surface of pure WO_3 NPs exhibits closely packed nanoplate structure as given in Fig. 3(a) [35]. On increasing the Cu^{2+} content from 5-20 wt%, nanoplates were transformed to irregular sphere-like NCs. This morphological change may occur due to the formation of $WO_3/CuWO_4$ nanocomposite [36]. The FESEM images of $WO_3/CuWO_4$ NCs shown in Fig. 3(b)-(e) evidently demonstrate that the particle size of sphere-like NCs decreases upon increasing the copper content and is in agreement with the decrease in crystallite size calculated from XRD analysis.

3. HRTEM Analysis

Morphology evolution of pure WO_3 and Cu including WO_3 samples was deeply investigated by TEM and HRTEM analysis, and the captured micrographs are depicted in Fig. 4, and 5, respectively. TEM pictures of as synthesized pure WO_3 NPs appearing as nanoplate-like structure with sharp edges, and mild agglomeration may be due to physisorption of individual WO_3 nanoplates [37]. Plate-like structure of WO_3 started disappearing gradually while copper was added in the synthesis. Micrographs of 5 wt% $WO_3/CuWO_4$ NCs appeared as lamellae-like structure with sub-angular edges and their edges were not sharp like pure WO_3. Lamellae with sub-angular edges were turned into sphere-like structure when the percentage of copper addition increased from 5 to 20%. Morphology of WO_3 samples synthesised in the presence of copper was dis-

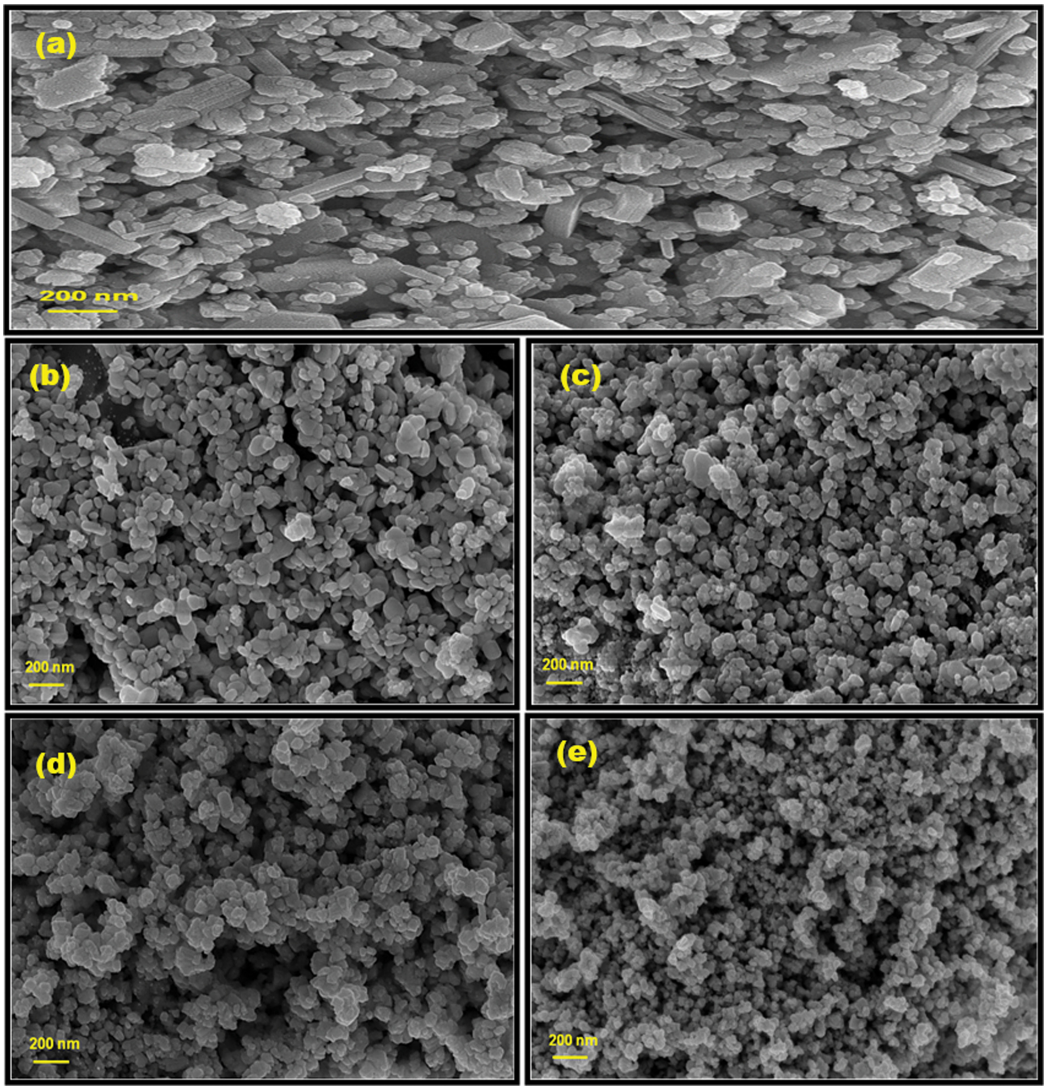

Fig. 3. FESEM images of (a) pure WO_3 nanoparticles and (b) 5 wt% Cu, (c) 10 wt% Cu, (d) 15 wt% Cu, and (e) 20 wt% Cu of $WO_3/CuWO_4$ nanocomposites.

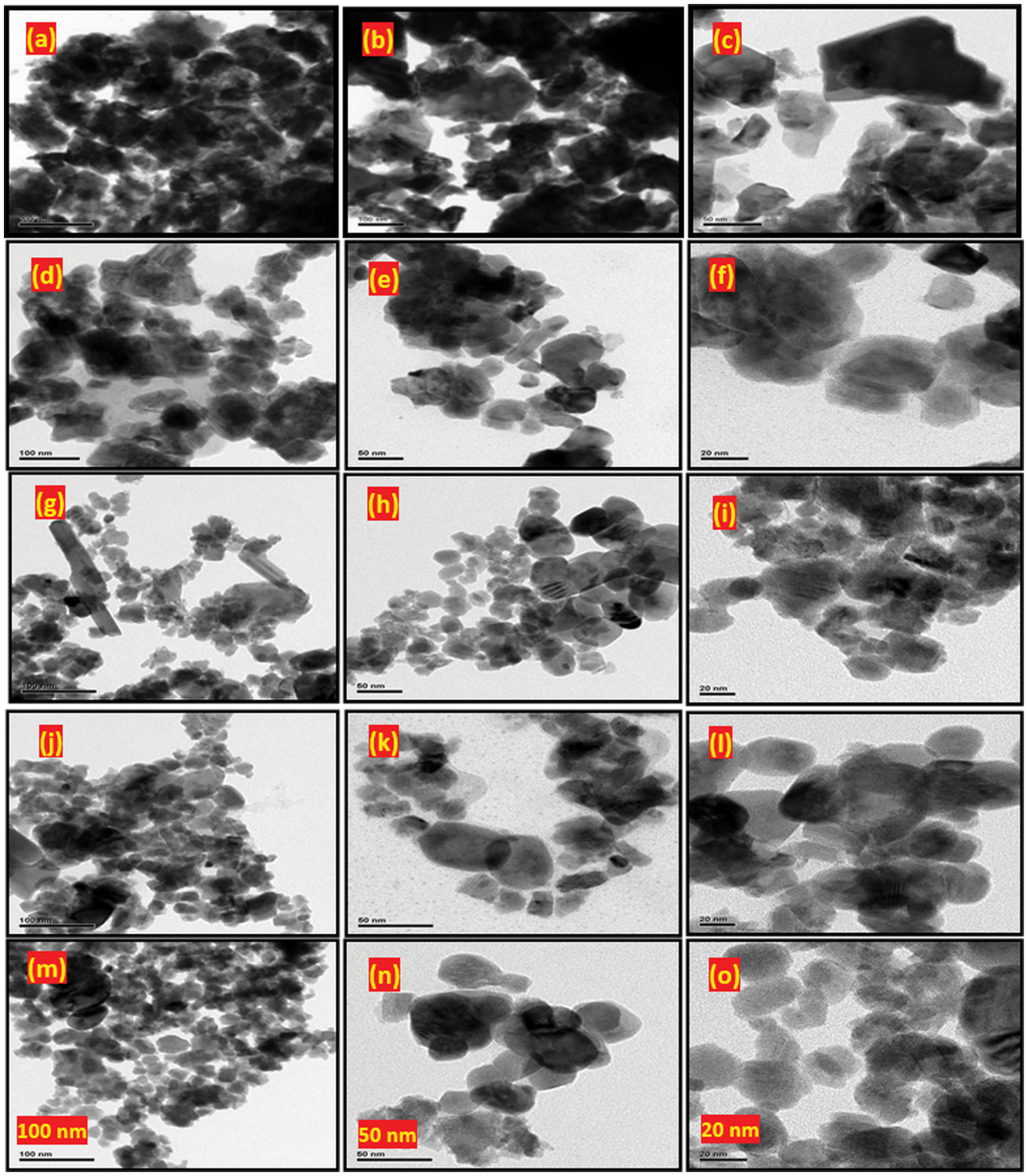

Fig. 4. TEM images of pure WO_3 nanoparticles (a)-(c), 5 wt% Cu (d)-(f), 10 wt% Cu (g)-(i), 15 wt% Cu (j)-(l) and 20 wt% Cu (m)-(o) of WO_3/$CuWO_4$ nanocomposites.

tinct and particle size was significantly reduced. Two different morphologies were observed in the WO_3/$CuWO_4$ samples, which may be clear classification of formation of WO_3 and $CuWO_4$, which is well matched with the XRD results.

HRTEM and SAED pattern images of pure WO_3 (Fig. 5(a) and (f)) confirmed the formation of the desired compound; the interplanar spacing 0.374 nm corresponds to the (020) plane of monoclinic WO_3 structure [38]. SAED pattern of pure samples clearly confirms the crystalline nature and well distinct scatter dots were observed. HRTEM micrographs of WO_3/$CuWO_4$ samples confirm the presence of WO_3 and $CuWO_4$ phases as mixture (Fig. 5(b), (c), (d) and (e)). It is clearly confirmed that WO_3 particles were formed first and the copper influence later formed the $CuWO_4$ particles in copper including WO_3 samples. There may be core/shell type WO_3/$CuWO_4$ structure, while increasing the copper concentration $CuWO_4$ domination was increased around the WO_3 particles. Interplanar spacing 0.37 and 0.28 nm matched with (020) of monoclinic WO_3 and triclinic (-111) planes of $CuWO_4$, respectively. Corresponding shade patterns (Fig. 5(g), (h), (i) and (j)) confirm the polycrystalline nature of WO_3/$CuWO_4$ samples and mixed phases. Diffracted dots indicate the presence of dominant planes of WO_3 and $CuWO_4$ structures.

4. EDS Analysis

The elemental analysis of pure WO_3 NPs and WO_3/$CuWO_4$ NCs was determined by EDX and attained profiles are given in Fig. 6. These profiles visibly indicate that pure WO_3 contain W & O peaks. Additionally, the EDS profile of WO_3/$CuWO_4$ NCs composed of tungsten, oxygen and copper atoms confirmed the presence of W,

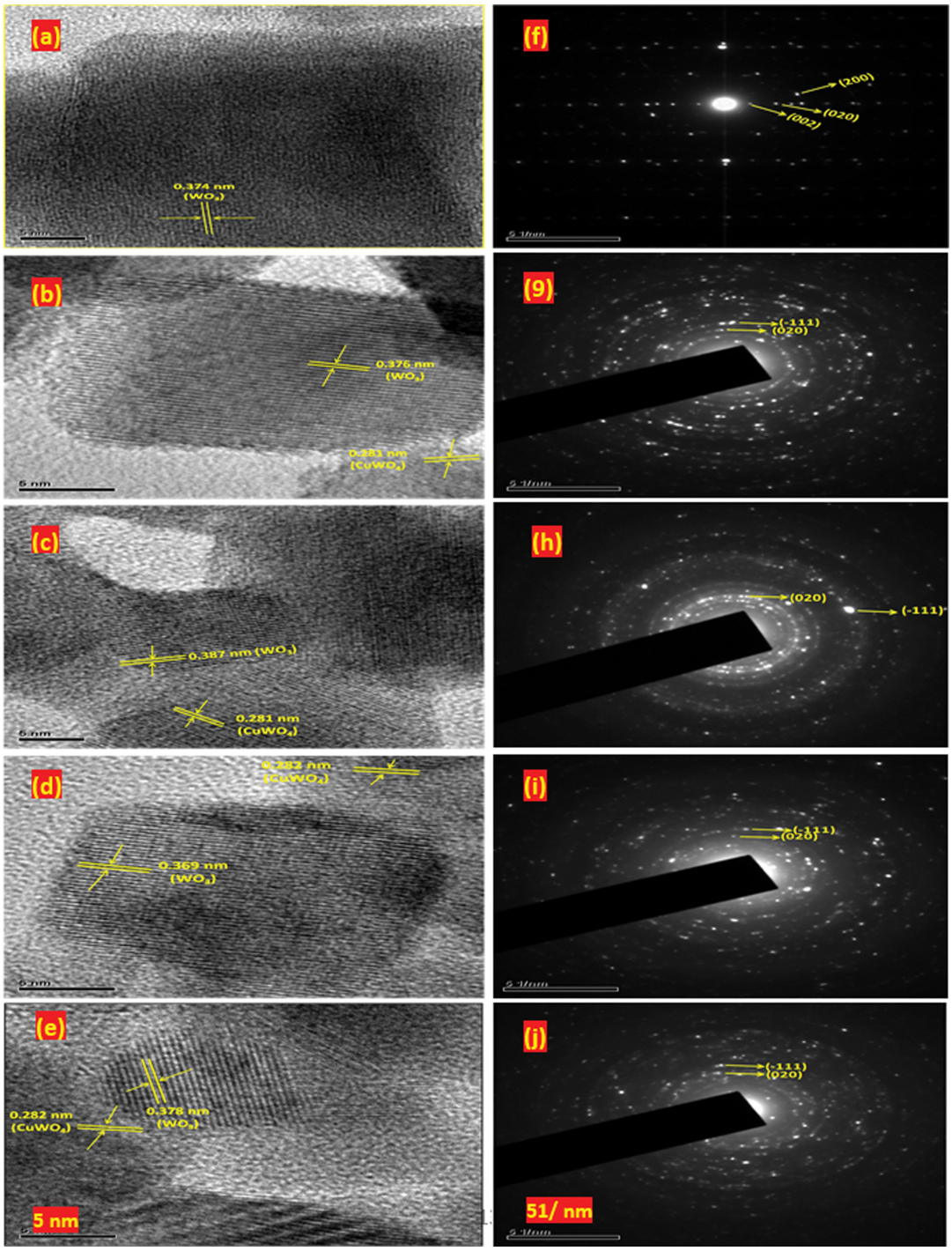

Fig. 5. HRTEM images with SAED pattern of pure WO_3 nanoparticles (a), (f), 5 wt% Cu (b), (g), 10 wt% Cu (c), (h), 15 wt% Cu (d), (i) and 20 wt% Cu (e), (j) of $WO_3/CuWO_4$ nanocomposites.

O and Cu atoms peaks. The compositional % of elements is given in the inset of Fig. 6. The intensity peak of tungsten was decreased due to the addition of Cu^{2+} in the tungsten site and atomic percentage of oxygen decreases gradually. This observation supports the photocatalytic performance due to the existence of deficiency ions in the prepared $WO_3/CuWO_4$ samples [39].

5. XPS Analysis

The measured XPS profiles for the prepared pure WO_3 and 20 wt% Cu@WO_3 samples are depicted in Fig. 7(a) and (b), respectively, and own the peaks for W, O, and Cu replicas [40]. Fig. 7(c) reveals the peaks for tungsten as W $4f_{5/2}$ and W $4f_{7/2}$ and for oxygen as O 1s as seen in Fig. 7(d). It is evident from Fig. 7(d), that the O 1s photoelectron peak is situated at ~531.2 eV, which is ascribed to the lattice oxygen of WO_3 crystal. However, when Cu was doped in WO_3 this peak was slightly shifted to 531.5 eV because of Cu doping in WO_3. For W the peaks assigned as W $4f_{5/2}$ and W $4f_{7/2}$

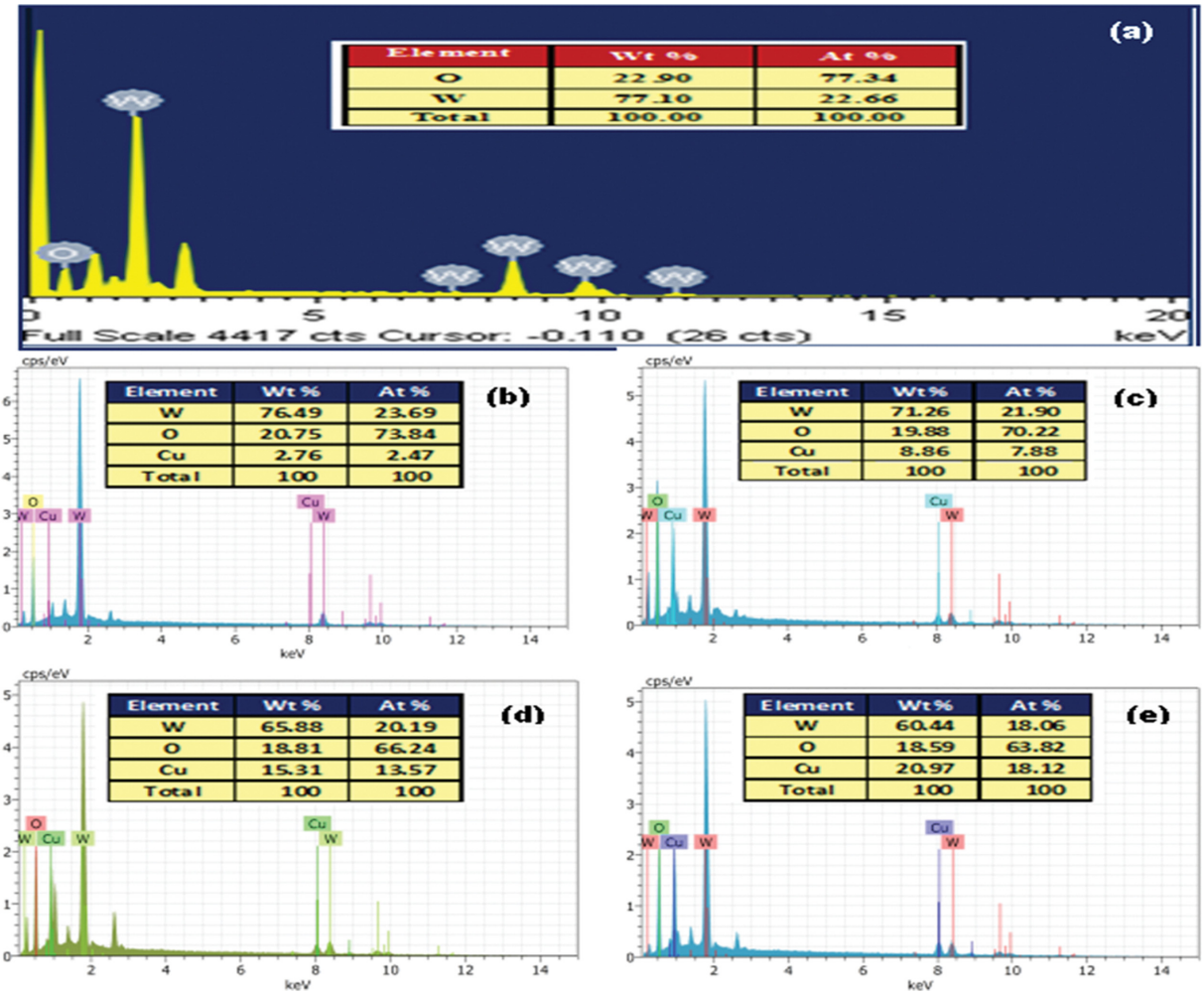

Fig. 6. EDAX spectra of (a) pure WO_3 nanoparticles and (b) 5 wt% Cu (c) 10 wt% Cu (d) 15 wt% Cu, and (e) 20 wt% Cu of WO_3/$CuWO_4$ nanocomposites.

are positioned at ~37.35 and 35.24 eV in pure and are slightly shifted to ~37.44 and 35.29 in WO_3/$CuWO_4$ NCs (see Fig. 7(c)). These peaks are reported at 38.2 and 36.94 eV in pure and are slight shifted to ~35.6 (or 35.7) and 37.8 (or 37.9) for Cu@WO_3 by Ghodselahi et al. [26]. Moreover, the Cu centers were also studied through XPS for knowing their electronic configuration in Cu $2p_{3/2}$ and Cu $2p_{1/2}$ area and depicted in Fig. 7(e). In this figure the Cu $2p_{3/2}$ related peaks are positioned at 934.31 eV and 941.58 eV and Cu $2p_{1/2}$ related peaks at 954.10 eV and 961.45 eV. Ghodselahi et al. reported the Cu $2p_{3/2}$ XPS peaks at ~935 eV [41]; however, Biesinger et al. reported the peak for Cu $2p_{3/2}$ at 932.61 eV [42]. However, to get exact and accurate energy peaks for related elements in XPS, a careful calibration needs to be done to avoid any error and also the product phases.

6. FTIR Studies

FT-IR profiles of WO_3 and WO_3/$CuWO_4$ NCs recorded at room temperature are shown in Fig. 8(a)-(e). The observed wavenumber from the recorded spectra and its corresponding assignments are demonstrated in Table 2. In WO_3 profile, the band at 634 cm^{-1} represents (W-O-W) stretching vibration. The band at 3,356-3,447 cm^{-1} resembles (O-H) stretching mode of WO_3/$CuWO_4$ NCs and the peaks at 1,619-1,625 cm^{-1} arise due to the (H-O-H) bending vibration mode of absorbed water present in pure and WO_3/$CuWO_4$ NCs. Further, the peaks at 712-727 cm^{-1} denote (O-W-O) stretching modes WO_3/$CuWO_4$ NCs. New distinct bands were observed at 913-921 and 555-564 cm^{-1} for the stretching vibration of (W-O) bonds in WO_4 tetrahedra in association with $CuWO_4$ phase. Moreover, the bands identified at 458-478 cm^{-1} represent symmetric stretching vibrations of CuO_6 octahedral phase. The FT-IR outcomes undoubtedly designate the presence of WO_3/$CuWO_4$ photocatalyst.

7. UV-Visible Studies

UV visible absorption, coefficient, reflectance and Kubelka-Munk (K-M) plot of pure and Cu included WO_3 are presented in Fig. 9(a)-(d). In absorption spectrum, excitonic feature of pure WO_3 starts around 500 nm, which is well matched with reported literature values [50]. Excitonic features of Cu including samples were gradually increased from 500 to 610 nm, which is evident that inclusion of Cu in the synthesis of WO_3 drastically changes in the optical and electronic structure of pure WO_3. Absorption coefficient (α) of 5% copper including WO_3 samples shows higher value (Fig. 9(b)), which was gradually lowering while increasing copper

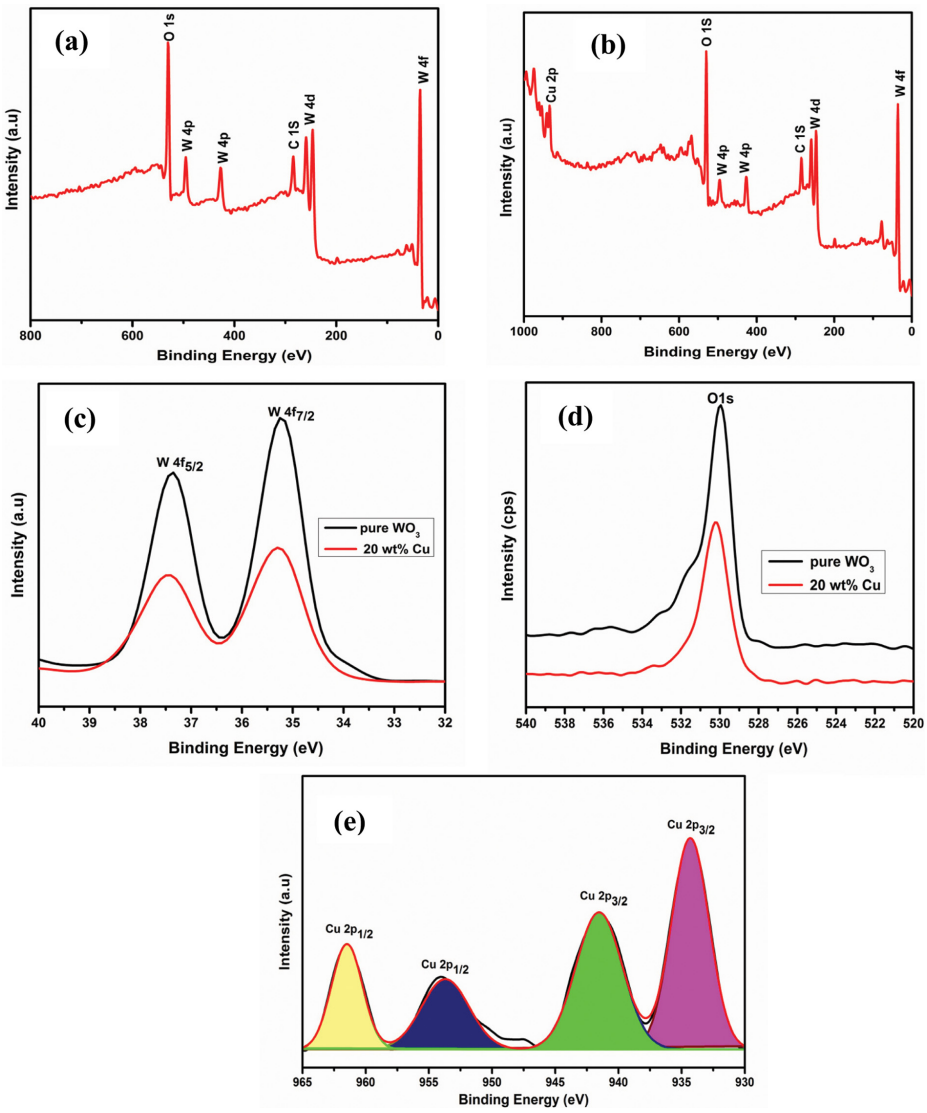

Fig. 7. (a) XPS survey spectra of pure WO_3 nanoparticles, (b) XPS survey spectra of 20 wt% Cu $WO_3/CuWO_4$ nanocomposites, (c), (d) High resolution XPS spectra of W4f and O1s of pure WO_3 nanoparticles, $WO_3/CuWO_4$ nanocomposites and (e) Cu 2p region of $WO_3/CuWO_4$ nanocomposites.

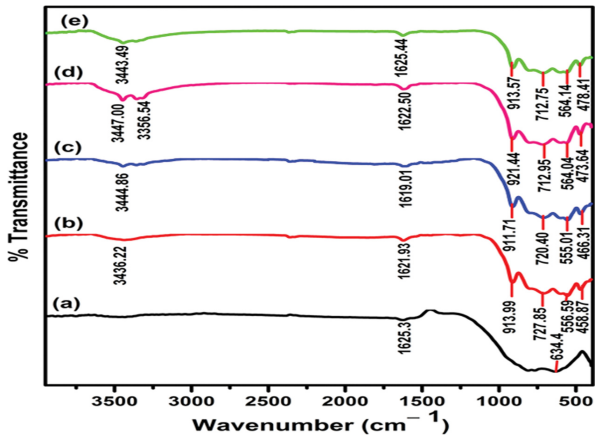

Fig. 8. FTIR spectra of (a) pure WO_3 nanoparticles (b) 5 wt% Cu (c) 10 wt% Cu (d) 15 wt% Cu, and (e) 20 wt% of Cu of $WO_3/CuWO_4$ nanocomposites.

ion percentage. The reflectance modifications were recorded and shown in Fig. 9(c) between 250 and 800 nm. From reflectance, E_g was calculated for each synthesized samples using Kubelka-Munk (K-M) rule through $(F(R)\,h\nu)^2$ vs. hv plot (Fig. 9(d)). The sketching of the linear section of the curve intercepts on X-axis, $((F(R)h\nu))^2 = 0$) provides the E_g values of samples. The procedure to get E_g is as follows:

$$F(R) = \frac{(1-R)^2}{2R} \tag{5}$$

where R is percentage reflectance.

Estimated band gaps of pure WO_3 NPs and $WO_3/CuWO_4$ NCs from Fig. 9(d) showed a continuous decrement while increasing the copper concentration from 2.6 to 2.25 eV. The details of the bandgap changes are given in Table 3.This means that wide bandgap pure WO_3 (inset in Fig. 9(d)) was transformed towards narrow bandgap while including Cu ions into it. Growth of $CuWO_4$

Table 2. Shows the vibrational band assignments for all absorption peaks in pure WO_3 nanoparticles and WO_3/$CuWO_4$ nanocomposites

Sample	pure WO_3	5 wt% Cu	10 wt% Cu	15 wt% Cu	20 wt% Cu	Assignment	References
Wavenumber (cm^{-1})	634	-	-	-	-	ν(W-O-W)	[43]
	-	458	466	473	478	ν(O-Cu-O)	[44]
	-	556	555	564	564	ν(W-O)	[45]
	-	727	720	712	712	ν(O-W-O)	[46]
	-	913	911	921	913	ν(W-O)	[47]
	1,625	1,621	1,619	1,622	1,625	δ(H-O-H)	[48]
	-	3,436	3,444	3,356	3,443	ν(OH)	[49]
	-	-	-	3,447	-	ν(OH)	[49]

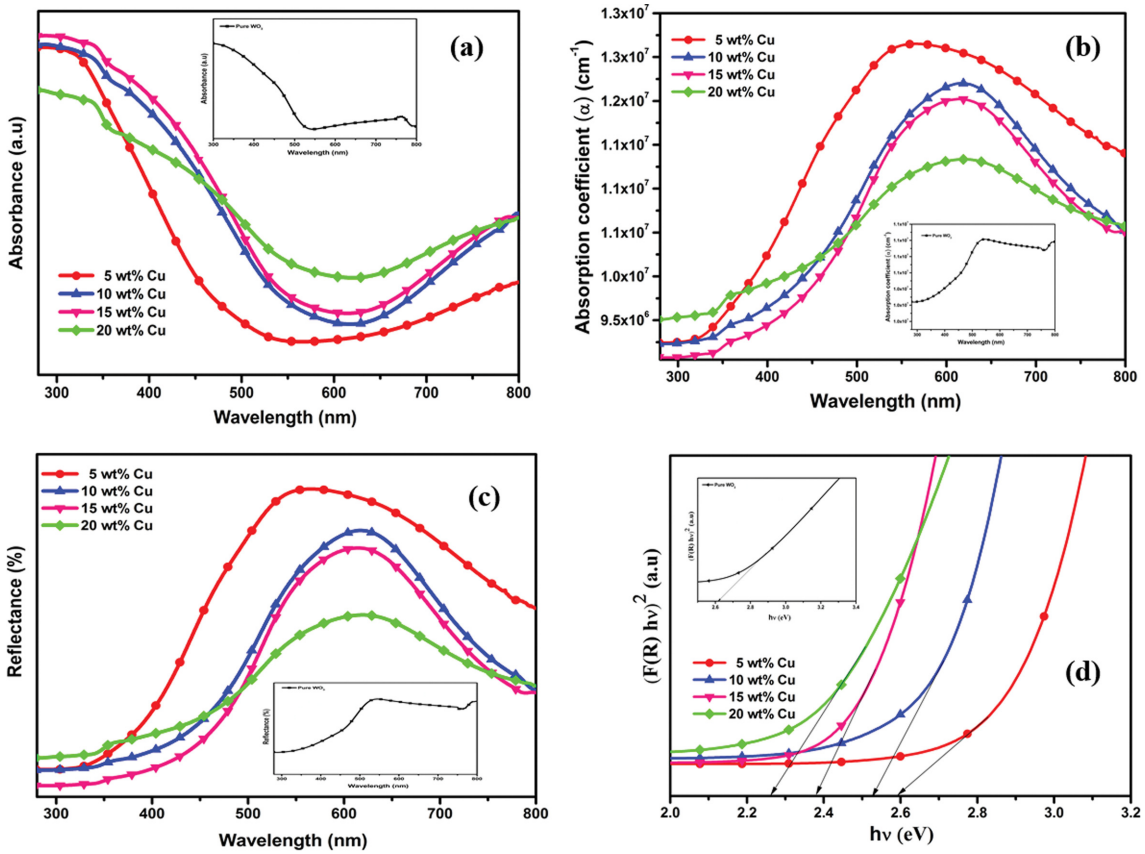

Fig. 9. (a) Absorbance spectra, (b) Absorption coefficient, (c) Diffuse Reflectance Spectra (DRS), and (d) K-M plot indicating the direct band gap for the corresponding reflectance spectra of pure WO_3 nanoparticles (inset) and WO_3/$CuWO_4$ nanocomposites.

Table 3. Estimated values of band gap for pure WO_3 and WO_3/$CuWO_4$ nanocomposites

Sample	Band gap (E_g) eV
pure WO_3	2.61
5 wt% Cu	2.59
10 wt% Cu	2.52
15 wt% Cu	2.37
20 wt% Cu	2.25

around WO_3 particles may be attributed to narrower band gap and increase in the excitonic feature of the Cu : WO_3. The reason is that bandgap report of $CuWO_4$ from the literature is 2.2-2.3 eV, while attempting to include Cu in the WO_3 system it is ended to new compound $CuWO_4$ instead of doping [51]. Since $CuWO_4$ completely covers the surface of the WO_3 particles, the bandgap is reduced to 2.25 eV for heavily Cu included samples.

8. Photoluminescence Studies

Photoluminescence of pure and Cu included WO_3 samples was measured under 280 nm excitation and recoded spectra between 350 and 500 nm are displayed in Fig. 10. Inset picture of Fig. 10 is the emission spectrum of pure WO_3 sample, which shows four high intensity emissions at 361, 383, 412, and 492 nm. Among them, the peak centered at 383 nm possesses the highest intensity. The emission peak at 361 nm may be generated due to near band edge transition and the rest of the low intense emissions such as 412

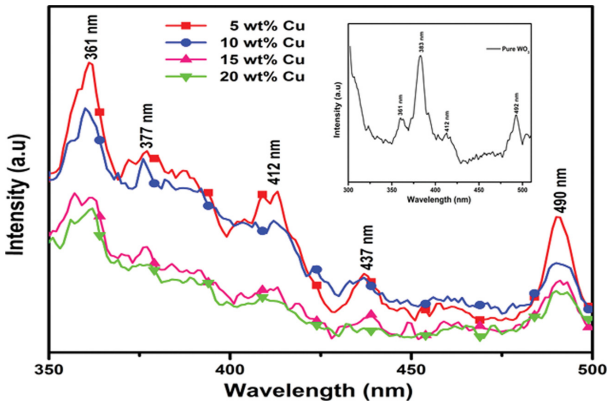

Fig. 10. Photoluminescence spectra of pure WO_3 NPs (inset) and $WO_3/CuWO_4$ nanocomposites.

and 492 nm may be raised from defect state originating between conduction band and valance band. The scenario of Cu included WO_3 samples is entirely changed [52]. In 5 wt% Cu, band edge transition emission at 361 nm intensity shows higher intensity than that of other emission features such as 377, 412, 437 and 490 nm. The intensity of emission peaks above discussed is getting decreased while increasing the copper concentration in the WO_3 synthesis. Principal emission peak of WO_3 completely vanished in highly Cu included samples and emission at 490 was retained even for high copper content in WO_3 samples. The reason is that the emission is raised from electronic transition within complex structure of WO_4^{2-} from newly formed $CuWO_4$ among WO_3 particles [53].

9. Photocatalytic Studies

The decolorization of MB dye in aqueous solution was performed beneath of UV-A light (365 nm) illumination and the UV-

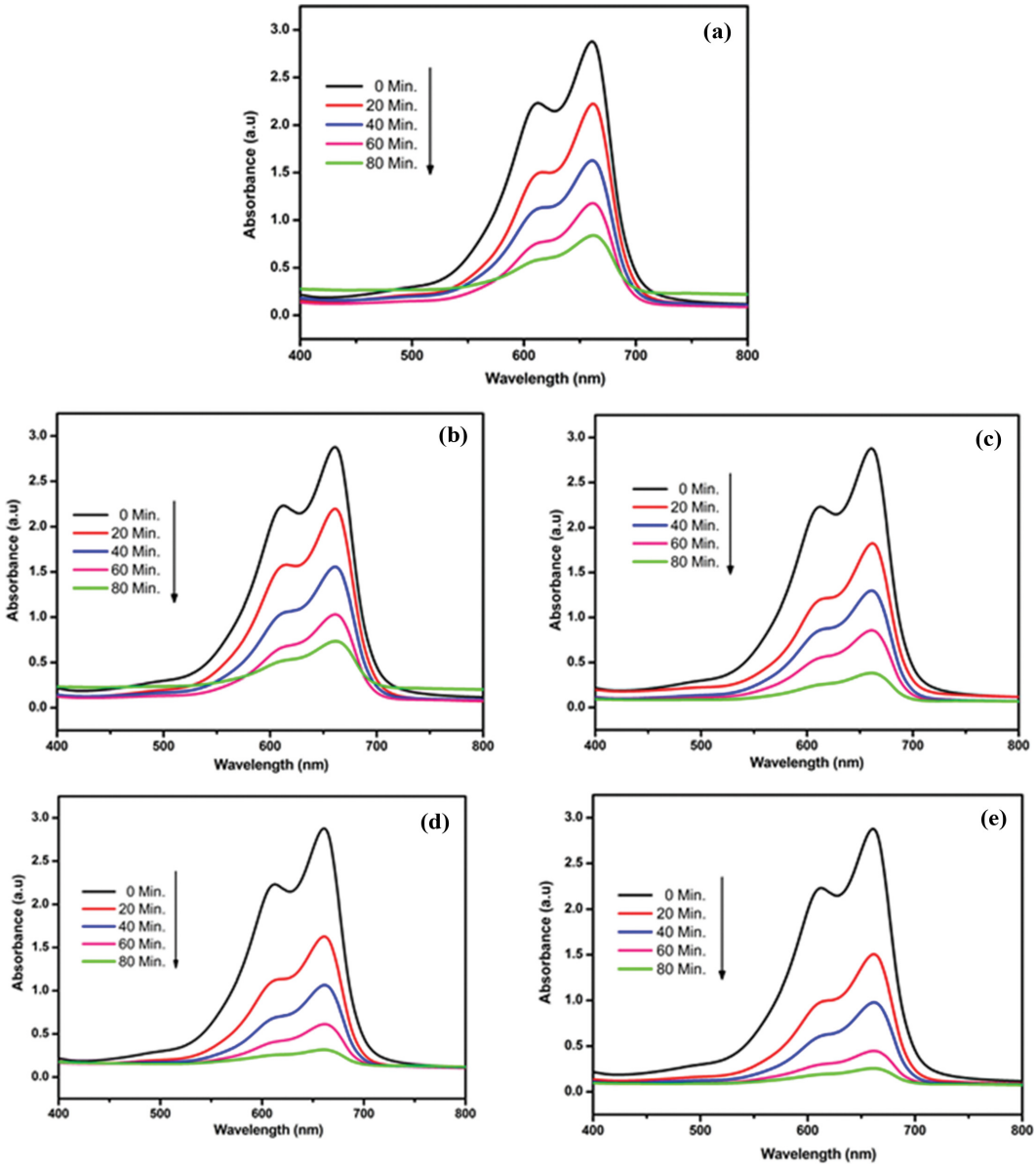

Fig. 11. The UV-Vis spectra of MB aqueous solution as a function of reaction time (a) pure WO_3 nanoparticles (b) 5 wt% Cu (c) 10 wt% Cu (d) 15 wt% Cu, and (e) 20 wt% of Cu of $WO_3/CuWO_4$ nanocomposites.

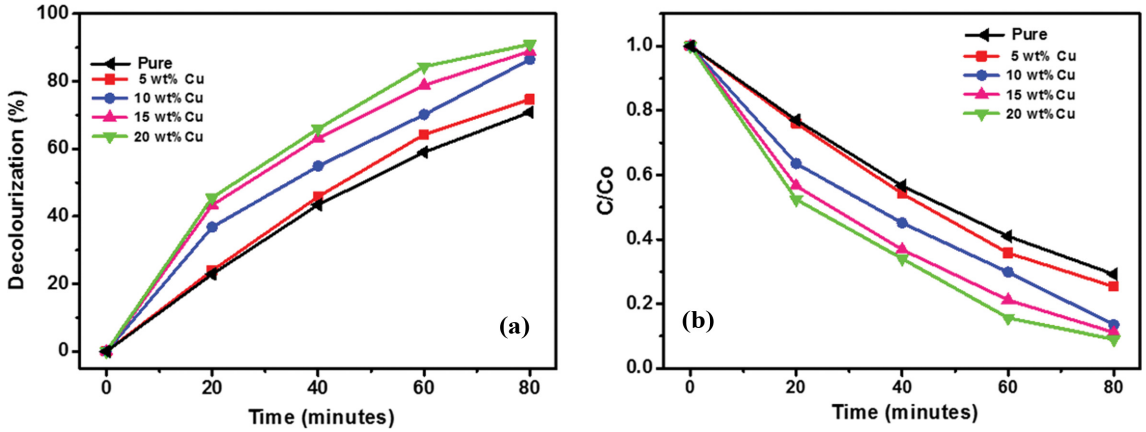

Fig. 12. (a) Methylene blue decolorization profile as a function of irradiation time, (b) relative absorbance curves of methylene blue (MB) decomposed photocatalytically by pure WO_3 nanoparticles and $WO_3/CuWO_4$ nanocomposites.

Table 4. Comparison of MB degradation efficiency of $WO_3/CuWO_4$ nanocomposites with other photocatalysts

Catalyst	Catalyst amount	MB concentration	Light source	Degradation%/time	Reference
WO_3/GN	60 mg	60 mL 350 ppm	15 W UV lamp	80/90 min	[54]
Nb doped WO_3	50 mg	10 mgl^{-1}	300 W Hg lamp	85/120 min	[55]
$WO_3/ZnWO_4$	100 mg	100 mL 1.0×10^{-4} M	35 W Xe lamp	55.54/480 min	[56]
WO_3/TiO_2	20 mg	25 $mmol\cdot m^{-3}$	230 W UV lamp	85/180 min	[57]
$CuWO_4$	40 mg	10 mg/L	300 W Xe lamp	86/90 min	[58]
$WO_3/CuWO_4$	0.02 g	10 mgL^{-1}	125 W Hg lamp	90.97/80 min	Present work

Visible spectrophotometer was used to control the reactions. Fig. 11(a)-(e) shows the UV-Vis. spectra of the decolorization of MB as a function of reaction time over different prepared photocatalysts at a constant interval time. As the irradiation time progresses, the absorption peak intensity gradually decreases from the maximum absorption value (661 nm). This progression indicates the MB dye degradation. The absorbance values of the dye suspension collected from 0-80 minutes interval can be re-expressed as a unit of concentration using the Lambert-Beer law.

$$\text{Decolorization Efficiency} = \frac{(C_0 - C)}{(C_0)} \times 100 \quad (6)$$

Here, C_0 & C stands for concentrations of MB dye (mgL^{-1}) before and after UV- A light irradiation.

The decolorization profiles of MB aqueous solution are presented in Fig. 12(a) and (b). Pure WO_3 was able to discharge 70% of original color of MB. When cupper incorporated into WO_3 the photocatalytic decolorization of MB was improved, the sample with 5 wt% Cu catalyzed the decolorization 74% of MB, while the sample 20 wt% Cu catalyzed the decolorization of 90% of MB. The photocatalytic degradation efficiency of $WO_3/CuWO_4$ nanocomposite was compared with the degradation of other photocatalysts reported in literature and the results are given in Table 4. The obtained results clearly show that all the Cu incorporated WO_3 samples exhibits better photocatalytic activity than that of pure WO_3. Moreover, a clear trend was obtained as the photocatalytic activity was increased with Cu content.

The pseudo-1st order reaction through a Langmuir-Hinshelwood (LH) rule was used to measure the degradation of dyes as follows.

$$\ln(C_0/C) = kt \quad (7)$$

Where, k is 1st-order rate constant and t stands for the time of irradiating the samples. Herein, the starting MB content was quite low (10 mgL^{-1}), so, the LH model was employed for evaluating k.

The obtained photocatalytic data were found to be fit with pseudo-first-order kinetic model in which $\ln(C_0/C)$ was plotted for all the reactions against the reaction time (min) (Fig. 13(a)). Straight lines were obtained with a high R^2 and therefore the slope represents a first-order rate constant (k) (Fig. 13(b)). The obtained kinetic data confirms the higher reaction rate associated with increasing Cu content in the prepared samples. The first-order rate constant of 20 wt% Cu sample exhibits two-times higher photocatalytic activity than pure WO_3. The obtained kinetic parameters are listed in Table 5.

Further, the decolorization efficiency of the prepared pure and doped catalysts was investigated by TOC (total organic carbon) analyzer and the results are shown in Fig. 14. This TOC removal efficiency graph clearly demonstrates the 20 wt% Cu doped WO_3 has the higher efficiency (68%) than other photocatalysts over the 80 min of light irradiation. The TOC removal efficiency of pure WO_3, 5 wt%, 10 wt% and 15 wt% Cu doped WO_3 was 12, 48, 55 and 62%, respectively.

10. Elemental Trapping Analysis

To confirm the reactive oxygen species for the decolorization reaction, the elemental trapping test was performed, and the results are displayed in Fig. 15. For the radicals trapping test benzoquinone (BQ), disodium ethylenediaminetetraacetic acid (EDTA), and

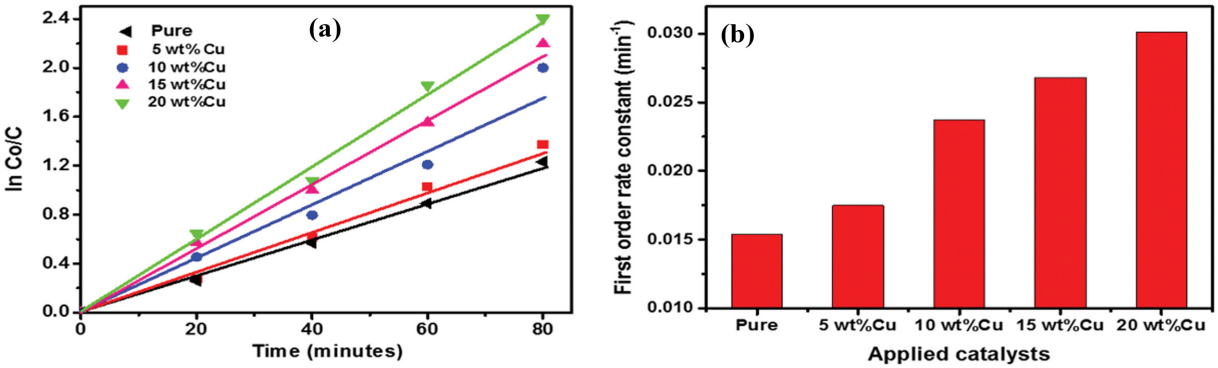

Fig. 13. (a) Pseudo-first-order kinetic plot for photo-decolorization of MB solution as a function of irradiation time. (b) The calculated first order rate constants of the applied catalysts.

Table 5. Parameters obtained from Pseudo - first - order kinetic plot for photo-decolorization of MB solution

Sample	Degradation efficiency (%)	Rate constant k (min^{-1})	Correlation coefficient (R^2)
pure WO_3	70.83	0.0154	0.9968
5 wt% Cu	74.65	0.0175	1.0000
10 wt% Cu	86.46	0.0237	0.9633
15 wt% Cu	88.89	0.0268	0.9945
20 wt% Cu	90.97	0.0301	0.9926

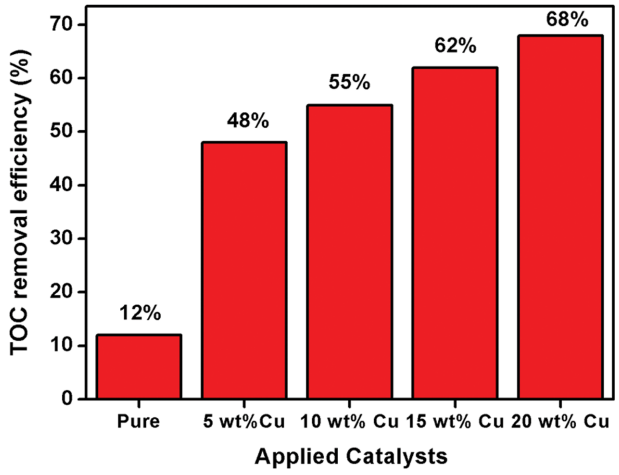

Fig. 14. TOC removal efficiency of prepared pure and Cu doped WO_3 catalysts.

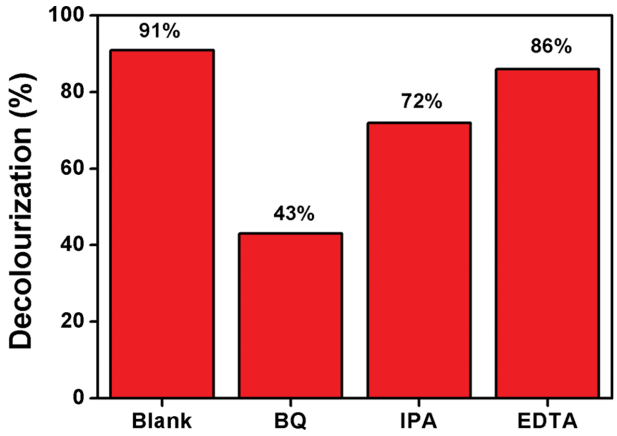

Fig. 15. Elemental trapping test for the prepared NCs of $WO_3/CuWO_4$.

isopropanol (IPA) were used as a superoxide radicals, holes and hydroxyl radicals, respectively [1,2,59-65]. The addition of BQ greatly reduces the decolorization efficiency up to 43% and it demonstrates that the superoxide radicals are the key active elements. Further the decolorization efficiency was decreased to 72% and 86% with addition of IPA and EDTA, respectively. Hence, from the elemental trapping experiment it could be observed that the superoxide radicals and hydroxyl radicals play the major and minor role for decolorization reaction.

11. Proposed Mechanism

As mentioned in the characterization results, the prepared catalysts can be considered nanocomposite of WO_3 and $CuWO_4$. Hence, to explain the photocatalytic activity of this composite, these two types of crystals must be considered in the explanation. First, pure WO_3 crystals can photocatalyze the reaction alone. Under the illumination of UV light, electron/hole pairs will be formed, electrons will be excited and move to CB while the holes will remain in valence band (VB). The holes can react with water to form $OH^{\cdot}$ radicals, which have strong option to react with the dye molecule and discharge their color. However, the photogenerated electrons and holes prefer to recombine instead of migrating to the surface to catalyze the photoreactions. This can explain the low photocatalytic activity of pure WO_3 crystals. However, in the case of $WO_3/CuWO_4$ nanocomposite, a heterojunction can take place between the two crystals. Under UV light illumination, electron/hole pairs will be formed in the two crystals (Fig. 16). Here, the excited electrons from $CuWO_4$ can travel to the CB of WO_3 while the holes in VB of WO_3 can travel to the VB of $CuWO_4$. This ensures the relatively long separation of electrons and holes and increases the chance for the photogenerated species to reach the surface of the crystals and perform the photocatalytic decolorization of MB. One additional factor can be added: the red shift in the bandgap of the composite which increased with increasing copper content means that the nanocomposite crystals can harvest photons from higher

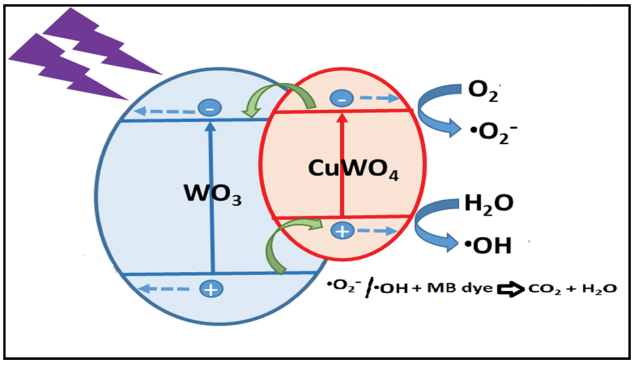

Fig. 16. The proposed mechanisms for the photocatalytic decolorization of MB dye under ultraviolet light illumination.

wavelength area of visible light. Similar explanation was proposed earlier by Chen et al. [22] and by Salimi et al. [20]. In this way the migrated electrons (at CB of WO_3) produce the superoxide radicals, whereas the holes (at VB of $CuWO_4$) oxidize the water and generate the hydroxyl radicals. These reactive radicals react with the dye molecules and produce the byproducts with releasing the CO_2 and H_2O [66].

CONCLUSION

Pure WO_3 NPs and WO_3/$CuWO_4$ NCs were successfully prepared by co-precipitation method. XRD studies confirmed the existence of monoclinic WO_3 as well as triclinic $CuWO_4$ structures. FESEM images demonstrated the transformation nanoplates to irregular sphere-like morphology. SAED dots indicates the presence of dominant plane of WO_3 (020) and $CuWO_4$ structures. The electronic configuration in pure WO_3, Cu $2p_{3/2}$ & Cu $2p_{1/2}$ doublet and its corresponding peak positions were identified through XPS. Estimated band gaps of pure WO_3 NPs as 2.61 eV and $CuWO_4$ completely covered the surface of the WO_3 particles, E_g was reduced to 2.25 eV for 20 wt% Cu NCs. From the elemental trapping experiment it could be observed that the superoxide radicals and hydroxyl radicals play the major and minor role for decolorization reaction. The TOC removal efficiency (68%) as well as first-order rate constant was two-times higher for 20 wt% WO_3/$CuWO_4$ NCs than pure WO_3 NPs.

ACKNOWLEDGEMENT

The author T. Thilagavathi would like to express her gratitude to Gobi Arts & Science College, Gobichettipalayam for providing laboratory facilities. The authors from KKU express their appreciation to the Deanship of Scientific Research at King Khalid University for funding this work through research groups program under grant number R.G.P.2/60/42.

REFERENCES

1. A. M. Saad, M. R. Abukhadra, S. Abdel-Kader Ahmed, A. M. Elzanaty, A. H. Mady, M. A. Betiha, J.-J. Shim and A. M. Rabie, *J. Environm. Manage.*, **258**, 110043 (2020).
2. M. R. Abukhadra, M. Shaban, F. Sayed and I. Saad, *Environ. Sci. Pollut. Res.*, **25**, 33264 (2018).
3. A. Yazdanbakhsh, A. Eslami, M. Massoudinejad and M. Avazpour, *Chem. Eng. J.*, **380**, 122497 (2020).
4. L. Kaliraj, J. C. Ahn, E. J. Rupa, S. Abid, J. Lu and D. C. Yang, *J. Photochem. Photobiol. B: Biol.*, **199**, 111588 (2019).
5. R. Abazari, A. R. Mahjoub, L. A. Saghatforoush and S. Sanati, *Mater. Lett.*, **133**, 208 (2014).
6. C. Lian, X. Xiao, Z. Chen, Y. Liu, E. Zhao, D. Wang and C. Chen, *Nano Res.*, **9**, 435 (2016).
7. T. D. Senguttuvan, V. Srivastava, J. S. Tawal, M. Mishra, S. Srivastava and K. Jain, *Sens. Actuat. B: Chem.*, **150**, 384 (2010).
8. M. Yan, Y. Wu, F. Zhu, Y. Hua and W. Shi, *Phys. Chem. Chem. Phys.*, **18**, 3308 (2016).
9. N. Dirany, M. Arab, V. Madigou, C. Leroux and J. R. Gavarri, *RSC Adv.*, **6**, 69615 (2016).
10. S. Salmaoui, F. Sediri, N. Gharbi, C. Perruchot, S. Aeiyach, I. A. Rutkowska, P. J. Kulesza and M. Jouini, *Appl. Surf. Sci.*, **257**, 8223 (2011).
11. X. Su, F. Xiao, Y. Li, J. Jian, Q. Sun and J. Wang, *Mater. Lett.*, **64**, 1232 (2010).
12. M. Szabó, P. Pusztai, A.-R. Leino, K. Kordás, Z. Kónya and Á. Kukovecz, *J. Molec. Struc.*, **1044**, 99 (2013).
13. M. Amini, B. Pourbadiei, T. P. A. Ruberu and L. K. Woo, *New J. Chem.*, **38**, 1250 (2014).
14. S. Cao, C. Zhao, T. Han and L. Peng, *Mater. Lett.*, **169**, 17 (2016).
15. B. Deepa and V. Rajendran, *Nano-Struct. & Nano-Obj.*, **16**, 185 (2018).
16. S. Lakshmiprabavathi, K. Govindan, K. Saravana Kumar, A. Jang and V. Muthuraj, *J. Indust. Eng. Chem.*, **80**, 558 (2019).
17. R. Mahdavi and S. S. A. Talesh, *Adv. Powder Technol.*, **28**, 1418 (2017).
18. M. Sajjad, I. Ullah, M. Khan, J. Khan, M. Y. Khan and M. T. Qureshi, *Res. Phys.*, **9**, 1301 (2018).
19. S. M. AlShehri, J. Ahmed, A. M. Alzahrani and T. Ahamad, *New J. Chem.*, **41**, 8178 (2017).
20. R. Salimi, A. A. Sabbagh Alvani, N. Naseri, S. F. Du and D. Poelman, *New J. Chem.*, **42** 11109 (2018).
21. N. F. A. Neto, Y. G. Oliveira, J. H. O. Nascimento, M. R. D. Bomio and F. V. Motta, *J. Mater. Sci. Mater. in Electron.*, **31** 18221 (2020).
22. H. Chen, X. Xiong, L. Hao, X. Zhang and Y. Xu, *Appl. Surf. Sci.*, **389**, 491 (2016).
23. I. Aslam, C. Cao, M. Tanveer, M. H. Farooq, W. S. Khan, M. Tahir, F. Idrees and S. Khalid, *RSC Adv.*, **5**, 6019 (2015).
24. M. B. Tahir, G. Nabi and N. R. Khalid, *Mater. Sci. Semicond. Proc.*, **84**, 36 (2018).
25. A. A. Ismail, M. Faisal and A. Al-Haddad, *J. Environm. Sci.*, **66**, 328 (2018).
26. C. Yu, F. Chen, Z. Liu, K. Yang, H. B. Ji, D. Li, W. Xie and S. Li, *J. Alloys Compd.*, **809**, 151844 (2019).
27. M. Shkir and S. AlFaify, *Sci. Rep.*, **7**, 16091 (2017).
28. M. Shkir, Z. R. Khan, T. Alshahrani, K. V. Chandekar, M. A. Manthrammel, A. Kumar and S. AlFaify, *Chin. Phys. B*, **29**, 116102 (2020).
29. M. Shkir, K. V. Chandekar, T. Alshahrani, A. Kumar, A. Khan and S. AlFaify, *The Europ. Phys. J. Plus*, **135**, 816 (2020).

30. M. Shkir, Z. R. Khan, K. V. Chandekar, T. Alshahrani, A. Kumar and S. AlFaify, *Appl. Nanosc.*, **10**, 3973 (2020).
31. K. Ravikumar, S. Agilan, M. Raja, R. Marnadu, T. Alshahrani, M. Shkir, M. Balaji and R. Ganesh, *Phys. B: Cond. Matt.*, **599**, 412452 (2020).
32. S. M. Mariappan, M. Shkir, T. Alshahrani, V. Elangovan, H. Algarni and S. AlFaify, *J. Alloys Compd.*, **22**, 157762 (2020).
33. F. Mehmood, J. Iqbal, A. Gul, W. Ahmed and M. Ismail, *Phys. E: Low-dim. Sys. Nanostruc.*, **88**, 188 (2017).
34. C. T. Nguyen, T. P. Pham, T. L. A. Luu, X. S. Nguyen, T. T. Nguyen, H. L. Nguyen and D. C. Nguyen, *Ceram. Intern.*, **46**, 8711 (2020).
35. D. J. Ham, A. Phuruangrat, S. Thongtem and J. S. Lee, *Chem. Eng. J.*, **165**, 365 (2010).
36. F. Duanmu, Z. Shen, Q. Liu, S. Zhong and H. Ji, *Chin. Chem. Lett.*, **31**, 1114 (2020).
37. J. Kaur, K. Anand, K. Anand and R. C. Singh, *J. Mater. Sci.*, **53**, 12894 (2018).
38. S.-J. Liu, Y. Yuan, S.-L. Zheng, J.-H. Zhang and Y. Wang, *Dalton Trans.*, **44**, 11360 (2015).
39. M. B. Tahir and M. Sagir, *Sep. Purif. Technol.*, **209**, 94 (2019).
40. S. Zhu, X. Liu, Z. Chen, C. Liu, C. Feng, J. Gu, Q. Liu and D. Zhang, *J. Mater. Chem.*, **20**, 9126 (2010).
41. T. Ghodselahi, M. A. Vesaghi, A. Shafiekhani, A. Baghizadeh and M. Lameii, *Appl. Surf. Sci.*, **255**, 2730 (2008).
42. M. C. Biesinger, L. W. M. Lau, A. R. Gerson and R. S. C. Smart, *Appl. Surf. Sci.*, **257**, 887 (2010).
43. R. Hatel and M. Baitoul, *Mater. Chem. Phys.*, **225**, 169 (2019).
44. E. L. S. Souza, J. C. Sczancoski, I. C. Nogueira, M. A. P. Almeida, M. O. Orlandi, M. S. Li, R. A. S. Luz, M. G. R. Filho, E. Longo and L. S. Cavalcante, *Ultras. Sonochem.*, **38**, 256 (2017).
45. M. Thiruppathi, K. Selvakumar, M. Arunpandian, K. Thirumalai, C. Ramalingan, M. Swaminathan and E. R. Nagarajan, *Colloid Surf. A: Phys. Eng. Asp.*, **563**, 148 (2019).
46. M. M. Mohamed, T. M. Salama, M. A. Hegazy, R. M. A. Shahba and S. H. Mohamed, *Int. J. Hydrogen Energy*, **44**, 4724 (2019).
47. S. Ramkumar and G. Rajarajan, *Appl. Phys. A.*, **123**, 401 (2017).
48. K. Jothivenkatachalam, S. Prabhu, A. Nithya and K. Jeganathan, *RSC Adv.*, **4**, 21221 (2014).
49. S. Shukla, S. Chaudhary, A. Umar, G. R. Chaudhary and S. K. Mehta, *Sens. Actuat. B: Chem.*, **196**, 231 (2014).
50. D. Li, D. Chandra, R. Takeuchi, T. Togashi, M. Kurihara, K. Saito, T. Yui and M. Yagi, *Chem. - A Europ. J.*, **23**, 6596 (2017).
51. N. Gaillard, Y. Chang, A. DeAngelis, S. Higgins and A. Braun, *Int. J. Hydrogen Energy*, **38**, 3166 (2013).
52. B. Ahmed, A. K. Ojha, A. Singh, F. Hirsch, I. Fischer, D. Patrice and A. Materny, *J. Hazard. Mater.*, **347**, 266 (2018).
53. S. M. Pourmortazavi, M. Rahimi-Nasrabadi, M. Khalilian-Shalamzari, H. R. Ghaeni and S. S. Hajimirsadeghi, *J. Inorg. Organomet. Poly. Mater.*, **24**, 333 (2014).
54. Y. Zhao, X. Wei, Y. Wang and F. Luo, *Chem. Phys. Lett.*, **607**, 34 (2014).
55. W. Mu, X. Xie, X. Li, R. Zhang, Q. Yu, K. Lv, H. Wei and Y. Jian, *RSC Adv.*, **4**, 36064 (2014).
56. Y. Keereeta, S. Thongtem and T. Thongtem, *Powder Technol.*, **284**, 85 (2015).
57. M. Ezaki, W. Michida and K. Kusakabe, *Trans. Tech. Publ.*, **6**, 293 (2014).
58. X. Hu, D. Gao, Y. Li, H. Dong, W. Zhou, L. Yang and Y. Zhang, *SN Appl. Sci.*, **1**, 119 (2018).
59. B. Palanivel, M. Lallimathi, B. Arjunkumar, M. Shkir, T. Alshahrani, K. S. Al-Namshah, M. S. Hamdy, S. Shanavas, M. Venkatachalam and G. Ramalingam, *J. Environ. Chem. Eng.*, **22**, 104698 (2020).
60. B. Palanivel, S. d. M. Perumal, T. Maiyalagan, V. Jayarman, C. Ayyappan and M. Alagiri, *Appl. Surf. Sci.*, **498**, 143807 (2019).
61. B. Palanivel and A. Mani, *ACS Omega*, **5**, 19747 (2020).
62. B. Palanivel, M. Shkir, T. Alshahrani and A. Mani, *Diam. Relat. Mater.*, **55**, 108148 (2020).
63. P. Kalisamy, M. Lallimathi, M. Suryamathi, B. Palanivel and M. Venkatachalam, *RSC Adv.*, **10**, 28365 (2020).
64. M. Lallimathi, P. Kalisamy, M. Suryamathi, T. Alshahrani, M. Shkir, M. Venkatachalam and B. Palanivel, *ChemistrySelect*, **5**, 10607 (2020).
65. R. Salimi, A. A. S. Alvani, N. Naseri, S. F. Du and D. Poelman, *New J. Chem.*, **42**, 11109 (2018).
66. B. Palanivel, C. Ayappan, V Jayaraman, S. Chidambaram, R. Maheswaran and A. Mani, *Mater. Sci. Semicond. Process.*, **100**, 87 (2019).